Study of turbid media with light: Recovery of mechanical and optical properties from boundary measurement of intensity autocorrelation of light

Hari. M. Varma,[1] A. K. Nandakumaran,[2] and R. M. Vasu[1,*]

[1]*Department of Instrumentation, Indian Institute of Science, Bangalore, 560012, India*
[2]*Department of Mathematics, Indian Institute of Science, Bangalore, 560012, India*
**Corresponding author: vasu@isu.iisc.ernet.in*

Received November 5, 2008; revised April 16, 2009; accepted April 17, 2009;
posted May 6, 2009 (Doc. ID 103700); published May 28, 2009

We discuss the inverse problem associated with the propagation of the field autocorrelation of light through a highly scattering object like tissue. In the first part of the work, we reconstruct the optical absorption coefficient μ_a and particle diffusion coefficient D_B from simulated measurements which are integrals of a quantity computed from the measured intensity and intensity autocorrelation $g_2(\tau)$ at the boundary. In the second part we recover the mean square displacement (MSD) distribution of particles in an inhomogeneous object from the sampled $g_2(\tau)$ measured on the boundary. From the MSD, we compute the storage and loss moduli distributions in the object. We have devised computationally easy methods to construct the sensitivity matrices which are used in the iterative reconstruction algorithms for recovering these parameters from the measurements. The results of the reconstruction of μ_a, D_B, MSD and the viscoelastic parameters, which are presented, show reasonably good position and quantitative accuracy.

OCIS codes: 170.3880, 170.3660, 170.3010, 170.4580, 100.3190, 350.5500.

1. INTRODUCTION

Temporal fluctuations of multiply scattered light in a turbid scattering medium have been used in the past to recover quantitative information on the dynamics of particles in the medium [1–3]. In a thick multiply scattering medium, light transport is essentially diffusive, and light emerging from such a medium presents a diffuse speckle field. Measurement of the intensity autocorrelation $g_2(\tau)$ of the exiting diffusive light and the extraction of the information regarding the dynamics of the medium through study of the propagation of the field correlation have resulted in the establishment of the technique of diffusing-wave spectroscopy (DWS). Measurement of the time dependence of $g_2(\tau)$ has been employed to study the types of movements the scattering particles undergo, such as temperature-induced Brownian motion [3], short-impulsive movement [4], sheer-flow [5], and movement introduced by external means such as ultrasound pressure [6,7]. The mean-square displacement (MSD) of scatterers $\langle \Delta r^2(\tau) \rangle$ undergoing Brownian motion is measured and made use of to extract the viscoelastic properties of the medium, which is either the background liquid in which tracer particles are added or a jellylike medium such as cross-linked polymers with aggregates acting as scattering particles. One of the advantages of DWS in this context is its ability to measure the individual movements of particles at shorter length and time scales than is considered possible by other means.

Application of diffuse light to probe a multiply scattering medium like tissue to recover spatially varying optical properties such as absorption coefficient μ_a and scattering coefficients μ_s is well established [8,9]. In this area, known as diffuse optical tomography (DOT), one makes multiple measurements of the photon flux of the emerging diffusive light to recover spatial distributions of μ_a and μ_s' (reduced scattering coefficient) employing a diffusion equation to model light propagation through the turbid medium. Over the years many have also successfully employed light to probe heterogeneous turbid media where the heterogeneity is in the movement or dynamics of the particles of the medium [10–12]. Here the multiple boundary measurements of $g_2(\tau)$ are made use of in conjunction with a propagation model for the basic field autocorrelation of light. This method has been used to image (or measure) shear flow through a capillary immersed in a turbid medium without flow [13] and to visualize or measure differential Brownian motion in a heterogeneous medium. In [11] a set of measurements of $g_2(\tau)$ has been employed to locate and reconstruct the particle diffusion coefficient D_B heterogeneity buried deep inside a multiply scattering object.

The MSD of particles in a medium has been used to study the rheological properties of the medium, for example, to measure the storage and the loss moduli of the medium in which the beads are embedded [14]. In a cross-linked polymer like polyvinyl alcohol, the MSD of the polymer aggregate has been used to recover the elastic and viscous moduli of the polymer itself [15]. Thus DWS has given us a localized probe for quantitative assessment of viscoelastic properties of turbid media confined to di-

mensions of the probe (millimeters or even micrometers), which saw the arrival of the applications of DWS for microrheology measurements [16].

The aim of the present work is the study of heterogeneous turbid media—heterogeneous in optical absorption coefficient and viscoelastic properties—with the help of a coherent light probe. The ultimate goal is medical diagnostic imaging of soft-tissue organs for cancer, where the cancerous region presents itself as an inhomogeneity in absorption coefficient and storage modulus. While reconstructing the viscoelastic properties of the medium through so-called diffuse correlation tomography (DCT) [17,18], we cannot claim the spatial resolution of microrheology, limited only by the dimensions of the probe beam. The diffusive propagation of light (and its field correlation) in the media precludes this, and the spatial resolution of the properties is restricted to typically the transport mean path l^* of the medium, which is of the order of 5–10 mm.

DCT has been tried and proven in the context of biomedical imaging. For example it has been employed to map blood flow in rat brain to study cortical spreading depression [17] and blood flow in the human brain [19] and in breast tumors [20]. However, to the best of our knowledge there has been no attempt to employ DCT to map the viscoelastic properties of soft tissue organs. Also, to the best of our knowledge the reconstruction methods adopted in earlier work [11,17] in this direction relied on the Rytov approximation with the underlying assumption that the heterogeneous distribution of the property to be reconstructed is only a small perturbation in its homogeneous background value. The data used in the recovery was either the full set of $g_2(\tau)$ versus τ distribution at various observation points or a single $g_2(\tau)$ value selected at τ when the effect of noise is minimal [17]. There was no proper development or analysis of an iterative reconstruction procedure involving the forward propagation of the basic quantity, namely, the field autocorrelation denoted by $g_1(\tau)$, nor computation of suitable Jacobians for the different measurement types derived from the measured $g_2(\tau)$, which could possibly recover both the mechanical [represented by $D_B(\mathbf{r})$, the particle diffusion coefficient, or the MSD itself] and optical property [represented by $\mu_a(\mathbf{r})$] distributions. We also show that from the measured $g_2(\tau)$ versus τ distribution it is possible to reconstruct $\langle \Delta r^2(\mathbf{r},\tau)\rangle$ of a heterogenous object.

Therefore one of the major aims of the present work is the development and testing of an iterative reconstruction algorithm similar to the iterative reconstruction algorithm of DOT [21] for use in the context of DCT. In the first part of this development we consider two measurements derived from $g_2(\tau)$ which are integrals of $\Gamma(\tau)$ computed from $g_2(\tau)$ (see Subsection 3.A) over intervals of τ. The first, denoted by M_1, is over the early part of τ, typically from $\tau=10^{-9}$ s to $\tau=10^{-7}$ s, and the second, M_2, is over the later part of τ, typically from $\tau=10^{-6}$ s to $\tau=10^{-3}$ s. When $\langle \Delta r^2(\mathbf{r},\tau)\rangle$ can be approximated by $6D_B\tau$ with a time independent particle diffusion coefficient (i.e., the medium is assumed purely viscous), we show that the measurement M_2 is sensitively dependent on D_B and can be recovered from M_2 without being affected by μ_a. Similarly M_1 is seen to be more sensitive to changes in $\mu_a(\mathbf{r})$ and can be used to recover $\mu_a(\mathbf{r})$. In the second part we recover the time variation of the spatial distribution of $\langle \Delta r^2(\mathbf{r},\tau)\rangle$ from the measured $g_2(\tau)$ versus τ distributions (and the intensity), assuming that the $\langle \Delta r^2(\mathbf{r},\tau)\rangle$ has a nonlinear dependence on τ. The recovered $\langle \Delta r^2(\mathbf{r},\tau)\rangle$ distributions at the inhomogeneities are also employed to compute the storage and loss moduli, denoted by $G'(\omega)$ and $G''(\omega)$, respectively, in those inhomogeneities [22].

Since the ultimate goal of the present work is the development of a medical imaging modality, we also suggest the limitations of this imaging method in the context of an experimental realization. We point out limits in noise in measurement which will allow a proper recovery of the properties of interest, touch upon spatial resolution of inhomogeneous inclusions recovered, and suggest practical data gathering geometry in a possible instrument.

A summary of the rest of the paper is as follows. In Section 2 we give a brief description of the forward propagation model used for $G(\mathbf{r},\tau)$, the unnormalized field correlation. We also study the sensitivity of the measurements M_1 and M_2 with respect to the parameters D_B and μ_a. In Section 3, we describe the construction of the Jacobians (or the sensitivity matrices) for M_1 and M_2 with respect to D_B and μ_a and $g_2(\tau)$ with respect to $\langle \Delta r^2(\mathbf{r},\tau)\rangle$. The inversion algorithms for the recovery of D_B, μ_a, and $\langle \Delta r^2(\mathbf{r},\tau)\rangle$ are described in Section 4. The numerical experiments revealing the ability of the inversion algorithm to reconstruct these parameters and their limitations, such as handling of noisy data, spatial resolution, and contrast recovery in the reconstruction, are described in Section 5. Section 6 contains a few suggestions on experimental layout for data gathering and possible limitations of the experiment and its effect on the ultimate recovery of the properties of the medium. The final Section 7, gives the conclusions drawn from this study.

2. FORWARD PROPAGATION EQUATION FOR THE FIELD AUTOCORRELATION THROUGH A TISSUELIKE MEDIUM

The basic quantity of interest to be propagated is the specific intensity $I(\mathbf{r},\hat{\mathbf{s}},\tau)$ (which is time independent under some assumptions [23,24]) related to the mutual coherence function of the electric field components $E_a(\mathbf{r}_a,t)$ and $E_b(\mathbf{r}_b,t+\tau)$, denoted by $\langle E_a(\mathbf{r}_a,t)E_b^*(\mathbf{r}_b,t+\tau)\rangle$. We note that $I(\mathbf{r},\hat{\mathbf{s}},\tau)$ is obtained from the mutual coherence function expressed using the center of gravity coordinates $\mathbf{r}=(\mathbf{r}_a+\mathbf{r}_b)/2$ and $\Delta\mathbf{r}=\mathbf{r}_b-\mathbf{r}_a$ after a Fourier transform with respect to $\Delta\mathbf{r}$ ($\hat{\mathbf{s}}$ is the conjugate variable to $\Delta\mathbf{r}$). The specific intensity obeys the correlation transport equation

$$\hat{\mathbf{s}}\cdot\nabla I(\mathbf{r},\hat{\mathbf{s}},\tau) = -\mu_t(\mathbf{r})I(\mathbf{r},\hat{\mathbf{s}},\tau) + \mu_s(\mathbf{r})\int I(\mathbf{r},\hat{\mathbf{s}}',\tau)g_1^s(\hat{\mathbf{s}},\hat{\mathbf{s}}',\tau)\mathrm{d}\hat{\mathbf{s}}' + S(\mathbf{r},\hat{\mathbf{s}}). \quad (1)$$

Here $\mu_t=\mu_a+\mu_s$, and $S(\mathbf{r},\hat{\mathbf{s}})$ is the source at the location $\mathbf{r}$. Also $g_1^s(\hat{\mathbf{s}},\hat{\mathbf{s}}',\tau)$ is the incremental specific intensity added in the direction $\hat{\mathbf{s}}$ owing to a single scattering event from direction $\hat{\mathbf{s}}'$ to $\hat{\mathbf{s}}$.

To get the diffusion approximation of the above transport equation, we expand $I(\mathbf{r},\hat{\mathbf{s}},\tau)$ as $I(\mathbf{r},\hat{\mathbf{s}},\tau)\approx G(\mathbf{r},\tau)+3\hat{\mathbf{s}}\cdot J(\mathbf{r},\tau)/4\pi$, where $G(\mathbf{r},\tau)$ and $J(\mathbf{r},\tau)$ are obtained from $I(\mathbf{r},\hat{\mathbf{s}},\tau)$ through $G(\mathbf{r},\tau)=\int I(\mathbf{r},\hat{\mathbf{s}},\tau)d\hat{\mathbf{s}}$ and $J(\mathbf{r},\tau)=\int\hat{\mathbf{s}}I(\mathbf{r},\hat{\mathbf{s}},\tau)d\hat{\mathbf{s}}$. The field autocorrelation $G(\mathbf{r},\tau)$ is related to the power spectrum of light through a Fourier transform with respect to τ. The diffusion approximation to Eq. (1) is obtained as (under the assumption that $\mu_s \gg \mu_a$) [12,24]

$$\nabla\cdot D(\mathbf{r})\nabla G(\mathbf{r},\tau)-\left(\mu_a(\mathbf{r})+\tfrac{1}{3}\langle\Delta r^2(\mathbf{r},\tau)\rangle k_0^2\mu_s'(\mathbf{r})\right)G(\mathbf{r},\tau) = -S_0(\mathbf{r}-\mathbf{r}_0), \tag{2}$$

where k_0 is the modulus of propagation vector of light; $\mu_s'=(1-g)\mu_s$, g being the anisotropic factor of scattering, and $D=1/3(\mu_a+\mu_s')$ is the optical diffusion coefficient. In the above model, we assume that the scattering is isotropic with a length scale $l^*=1/\mu_s'$. The term $S_0(\mathbf{r}-\mathbf{r}_0)$ is the isotropic source located at $\mathbf{r}=\mathbf{r}_0$. We use the mixed boundary condition to solve the propagation Eq. (2) for $G(\mathbf{r},\tau)$,

$$D(\mathbf{r})\frac{\partial G(\mathbf{r},\tau)}{\partial\mathbf{n}}=-G(\mathbf{r},\tau), \tag{3}$$

on the boundary $\partial\Omega$. Here $\mathbf{n}$ is the unit outward normal on $\partial\Omega$ where measurement is made. This implies that the light input is from the source at $\mathbf{r}_0$ only.

If we assume the medium is purely viscous, so that the scattering particles are pictured to diffuse through the medium, the MSD, $\langle\Delta r^2(\mathbf{r},\tau)\rangle$, at a particular $\mathbf{r}$ has a linear time evolution given by $\langle\Delta r^2(\mathbf{r},\tau)\rangle=6D_B(\mathbf{r})\tau$ [17], where $D_B(\mathbf{r})$ is the time independent particle diffusion coefficient related to the viscosity η of the medium. If the medium is viscoelastic, $\langle\Delta r^2(\mathbf{r},\tau)\rangle$ has a nonlinear τ dependence. For the viscoelastic medium used in our simulations, we have assumed [25]

$$\langle\Delta r^2(\mathbf{r},\tau)\rangle=r_0^2(\mathbf{r})\{1-\exp[(-\tau/\tau_d)^\alpha]\}^{1/\alpha}(1+6D_1\tau/r_0^2),$$

the recovery of which leads to the reconstruction of the complex elastic modulus of the medium.

This model has the flexibility to incorporate three different types of movement of a particle trapped in a viscoelastic network. In the first phase when τ is small the particle follows a diffusive motion with an MSD varying linearly with τ as $6D_B\tau$. When τ increases the $\Delta r^2(\mathbf{r},\tau)$ versus τ behavior becomes nonlinear, and at intermediate times it displays a plateau where the MSD becomes constant at r_0^2. At still larger values of τ the movement of the particles becomes diffusive again, showing a linear behavior of MSD with τ.

For the two cases of a purely viscous medium as well as the soft tissue-like viscoelastic medium, we solve Eqs. (2) and (3) using the finite element (FE) discretization scheme. A 2-D circular object is assumed and discretized to 1933 nodes with 3723 elements. The typical solution of $G(\mathbf{r},\tau)$ for $\tau=10^{-9}$ s to $\tau=10^{-2}$ s is shown in Fig. 1. We mention here in passing that $G(\mathbf{r},\tau)$ is not our measurement, but $g_2(\tau)$ and the intensity $I(\mathbf{r})=G(\mathbf{r},0)$ are. From these measurements we derive a quantity $\Gamma(\mathbf{r},\tau)$ as discussed in Subsection 3.A. We have assumed the optical parameters D and μ_s' are uniform with values given by 0.0417 cm and 8 cm^{-1}, respectively. Optical absorption coefficient μ_a has a background value of 10^{-3} cm^{-1}. Particle diffusion coefficient D_B has a background value 0.1×10^{-8} cm^2/s. The forward operator is used to compute $G(\mathbf{r},\tau)$ everywhere, especially on the boundary $\partial\Omega$.

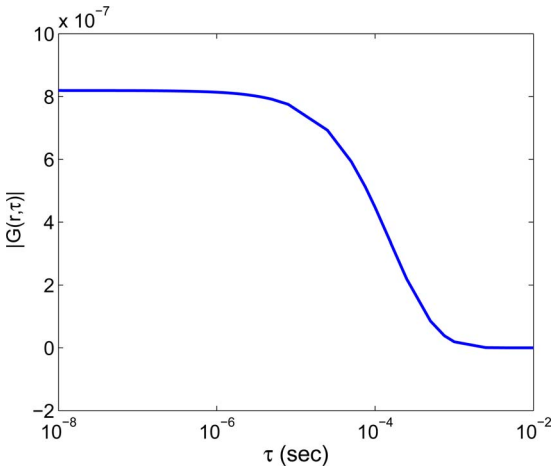

Fig. 1. (Color online) Typical plot of the modulus of field autocorrelation with τ at a boundary node for a homogeneous object: $\mu_a^b=0.001$ cm^{-1}, $\mu_s'^b=8$ cm^{-1}, and $D_B=0.1\times10^{-8}\text{cm}^2/\text{s}$.

The intensity autocorrelation, one of the measurements made on $\partial\Omega$, is given by

$$\langle I(\mathbf{r},\tau)I(\mathbf{r},t+\tau)\rangle\equiv g_2(\tau)=1+\beta|g_1(\mathbf{r},\tau)|^2. \tag{4}$$

Here $|g_1(\mathbf{r},\tau)|=|\frac{G(\mathbf{r},\tau)}{G(\mathbf{r},0)}|$, and β is a constant dependent on the collection optics used in the experiments. Since $G(\mathbf{r},0)$ is the intensity $I(\mathbf{r})$, which is also experimentally measured, we can arrive at $g_2(\tau)=1+\beta|G(\mathbf{r},\tau)/G(\mathbf{r},0)|^2$ from the computed $G(\mathbf{r},\tau)$.

3. MEASUREMENTS DERIVED FROM $g_2(\tau)$ AND THE VERIFICATION OF THEIR SENSITIVITIES WITH RESPECT TO D_B AND μ_a

A. Numerical Study of the Variation of the Measurements Derived from $g_2(\tau)$ with Absorption and Particle Diffusion Coefficients

First we consider the case of a purely viscous medium in which the approximation $\langle\Delta r^2(\mathbf{r},\tau)\rangle=6D_B(\mathbf{r})\tau$ holds. In this case the propagation equation for $G(\mathbf{r},\tau)$ has coefficients dependent on optical absorption coefficient μ_a, particle diffusion coefficient D_B and reduced scattering coefficient μ_s'. Of these, we assume μ_s' is known and uniform throughout the object, leaving us with two unknowns $\mu_a(\mathbf{r})$ and $D_B(\mathbf{r})$. Since our measurement is $g_2(\tau)\equiv M=1+\beta|G(\mathbf{m},\tau)/G(\mathbf{m},0)|^2$, and the propagation equation is for $G(\mathbf{r},\tau)$ we define a measurement operator $\mathcal{M}$ as

$$\mathcal{M}\{G(\mathbf{m},\tau)\}\equiv G^2(\mathbf{m},0)\left(\frac{M-1}{\beta}\right)\equiv\Gamma(\mathbf{m},\tau). \tag{5}$$

Here $\mathbf{m}$ is the detector location on $\partial\Omega$ the boundary. As indicated earlier $\Gamma(\mathbf{m},\tau)$ can be computed from boundary measurements. From $\Gamma(\mathbf{m},\tau)$ we derive a scalar measurement

$$M = \int_{\tau_1}^{\tau_2} \Gamma(\mathbf{m}, \tau) \mathrm{d}\tau, \tag{6}$$

where τ_1 and τ_2 define an interval on the τ axis within the support of $g_2(\tau)$. By numerical experiments we have selected two intervals, one in the neighborhood of $\tau=0$ (relatively small values of τ) and the other in the neighborhood of $\tau \approx 10^{-6}$ s (i.e., for larger values of τ), and used these measurements M_1 and M_2, respectively, to explore the possibility of reconstructing μ_a and D_B separately. As indicated in Section 1, we found that M_1 (where τ_1 and τ_2 are, respectively, 10^{-9} s and 10^{-7} s, and these values are fixed through repeated numerical simulations) is very sensitive to changes in μ_a and insensitive to changes in D_B, while M_2 (where τ_1 and τ_2 are, respectively, 10^{-6} s and 10^{-3} s) is very sensitive to changes in D_B and insensitive to changes in μ_a.

These factors were established using the following numerical experiments. We have considered a circular 2-D object of diameter 8 cm and homogeneous properties of $\mu_a=0.001$ cm^{-1} and $\mu_s'=8$ cm^{-1} and $D_B=0.1\times10^{-8}$ cm^2/s. After finite element discretization of Eq. (2) and Eq. (3) with 1933 nodes and 3723 elements we have solved for $G(\mathbf{r},\tau)$ everywhere in Ω and computed $\Gamma(\mathbf{m},\tau)$ on the boundary from which M_1 and M_2 were calculated. The measurements $\Gamma(\mathbf{m},\tau)$ evaluated at a typical detector point on the boundary when the homogeneous value of μ_a is varied from 0.001 to 0.01 cm^{-1} are shown in Fig. 2(a) (D_B is held constant at 0.1×10^{-8} cm^2/s). Similar curves showing $G(\mathbf{m},\tau)$ versus τ as D_B is varied from 0.1×10^{-8} cm^2/s to 1×10^{-8} cm^2/s (μ_a held constant at 0.001 cm^{-1}) are shown in Fig. 2(b).

It is clear from these figures that when τ is small (in the range of 10^{-9} s to 10^{-7} s), whereas D_B did not have any noticeable effect on $\Gamma(\mathbf{m},\tau)$, μ_a did have. The opposite is found to be true for larger values of τ. From these numerical trial runs we fix the values of τ_1 and τ_2 to arrive at the two intervals indicated earlier to compute the two measurements M_1 and M_2 using Eq. (6). The behavior of M_1 and M_2 with μ_a and D_B are shown in Figs. 3(a)–3(d). The earlier observations of the sensitivity of M_1 and M_2 to parameters μ_a and D_B are once again confirmed through the above results, and these measurements are subsequently used to reconstruct μ_a and D_B.

In Subsection 3.B we derive the sensitivity relations for measurements M_1 and M_2 with respect to μ_a and D_B. For the viscoelastic medium, the set of measurements $\{\Gamma(\mathbf{m},\tau_i)\}$ at a number of points on the boundary of the object sampled in τ starting from $\tau=10^{-9}$ to $\tau=10^{-2}$ s is used as data for the recovery of $\langle\Delta r^2(\mathbf{r},\tau)\rangle$. The sensitivity of $\Gamma(\mathbf{r},\tau)$ with respect to $\langle\Delta r^2(\mathbf{r},\tau)\rangle$ is established quantitatively, and the corresponding sensitivity matrix is also computed.

B. Construction of the Jacobian for the Measurements M_1 and M_2 with Respect to μ_a and D_B

We intend to employ a forward-propagation-model-based iterative reconstruction algorithm to recover μ_a and D_B, which requires repeated computation of the derivative (sensitivity or Jacobian matrix) of the measurements with respect to the parameters to be reconstructed. To this end we describe here a method for the quick evaluation of these Jacobian matrices [26,27]. The iterative reconstruction procedure essentially involves comparison of the experimental measurements with the computed measurements obtained via the forward operator and perturbing the material properties, guided by the Jacobians.

1. Jacobian with Respect to Absorption Coefficient

Using Eq. (2), which is the forward propagation equation for the basic quantity $G(\mathbf{r},\tau)$, one can compute a perturbation in $G(\mathbf{r},\tau)$, by say $G^\delta(\mathbf{r},\tau)$, by perturbing $\mu_a(\mathbf{r})$ by $\mu_a^\delta(\mathbf{r})$. Substituting these in Eq. (2), after simplification we get the equation connecting $G^\delta(\mathbf{r},\tau)$ to $\mu_a^\delta(\mathbf{r},\tau)$, which we call the Frechet derivative of the forward propagation equation:

$$\nabla\cdot D\nabla G^\delta(\mathbf{r},\tau) - (\mu_a + 2D_B\tau k_0^2\mu_s')G^\delta(\mathbf{r},\tau) = \mu_a^\delta G(\mathbf{r},\tau). \tag{7}$$

The boundary condition for $G^\delta(\mathbf{r},\tau)$ is

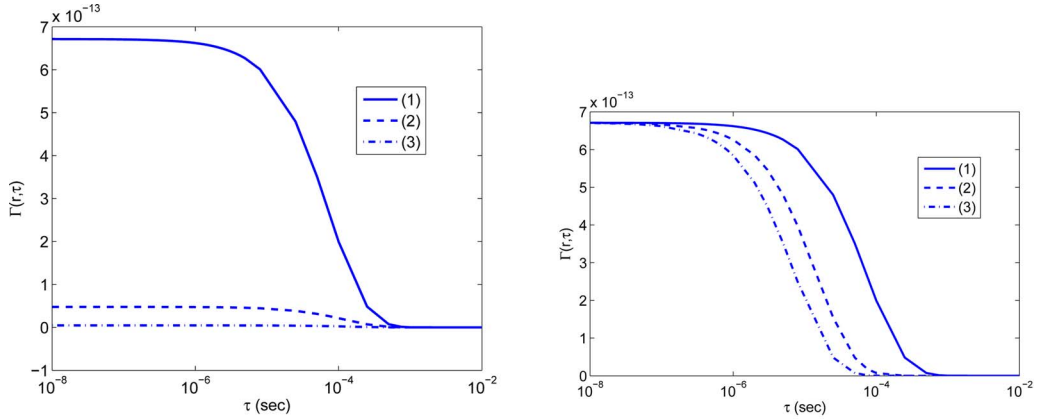

Fig. 2. (Color online) Plots of $\Gamma(\mathbf{r},\tau)$ versus τ when: (a) background μ_a is varied from (1) 0.001 cm^{-1} to (2) 0.005 cm^{-1}, (3) 0.01 cm^{-1}, D_B remaining constant at 0.1×10^{-8} cm^2/s; (b) background D_B is varied from (1) 0.1×10^{-8} cm^2/s to (2) 0.5×10^{-8} cm^2/s, (3) 1×10^{-8} cm^2/s, μ_a remaining constant at 0.001 cm^{-1}. The source–detector separation used in the simulation was 8 cm.

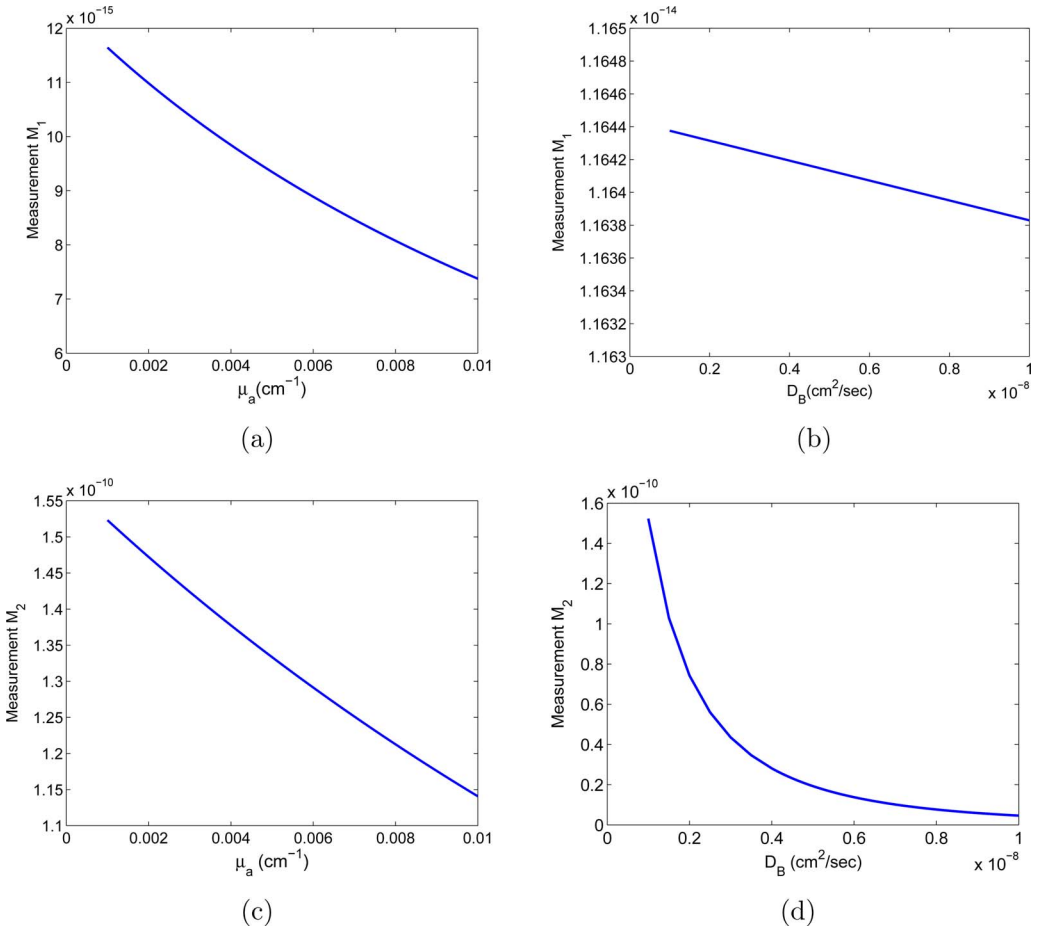

Fig. 3. (Color online) Variations of M_1 and M_2 with μ_a and D_B. (a) M_1 versus μ_a, (b) M_1 versus D_B, (c) M_2 versus μ_a, (d) M_2 versus D_B. It is seen that M_1 and M_2 have larger variations with respect to μ_a and D_B, respectively

$$G^{\delta}(\mathbf{m},\tau) + D\frac{\partial G^{\delta}(\mathbf{m},\tau)}{\partial n} = 0, \qquad \mathbf{m} \in \partial\Omega. \tag{8}$$

Solution of Eqs. (7) and (8) gives $G^{\delta}(\mathbf{r},\tau)$, in particular on the boundary, for μ_a perturbation, say at a node. On $G^{\delta}(\mathbf{m},\tau)$ we apply the measurement operator $\mathcal{M}$ [Eq. (5)] to obtain $\Gamma^{\delta}(\mathbf{m},\tau)$, from which the change in measurement M^{δ} is computed as $M^{\delta}=\int_{\tau_1}^{\tau_2}\Gamma^{\delta}(\mathbf{m},\tau)\mathrm{d}\tau$. We use this to compute the derivative, the rate of change of a measurement with respect to μ_a at a node, which is an element of the Jacobian matrix with respect to μ_a. The whole matrix can be evaluated by continuing these calculations for all nodes and for all detectors.

This rather computation-intensive procedure can be avoided by employing the adjoint of the Frechet derivative operator [Eqs. (7) and (8)], as is done in the context of DOT [26,27]. With this, one can get a row of the Jacobian matrix (i.e., the derivative for a single measurement with respect to the parameter at all the nodes) by solving two forward propagation operators, one, Eqs. (7) and (8), and the other its adjoint.

The adjoint of Eqs. (7) and (8) can be easily found as

$$\nabla\cdot D\,\nabla\,\psi(\mathbf{r},\tau) - (\mu_a + 2D_B\tau k_0^2\mu_s')\psi(\mathbf{r},\tau) = 0, \tag{9}$$

with the boundary condition

$$\psi(\mathbf{r},\tau) + D\frac{\partial\psi(\mathbf{r},\tau)}{\partial n} = q^{+}. \tag{10}$$

Here q^{+} is the so-called "Robin source" at the boundary where the detector is located [26].

Multiplying Eq. (7) by $\bar{\psi}$ and Eq. (9) by $G^{\delta}(\mathbf{r},\tau)$, integrating over the whole domain Ω, and applying Green's theorem, we get

$$\int_{\partial\Omega} G^{\delta}(\mathbf{m},\tau)q^{+}\mathrm{d}^{n-1}r = \int_{\Omega}\mu_a^{\delta}(\mathbf{r})G(\mathbf{r},\tau)\psi(\mathbf{r},\tau)\mathrm{d}^{n}r. \tag{11}$$

If q^{+} is a delta source at the detector on the boundary, the left hand side of Eq. (11) picks up a $G^{\delta}(\mathbf{m},\tau)$ at the detector. In that sense Eqs. (9) and (10) together represent the adjoint of Eqs. (7) and (8).

We make use of Eq. (11) and Eq. (7) to arrive at an expression for $\partial\Gamma^{\delta}(\mathbf{m},\tau)/\partial\mu_a$ for μ_a at every node. Here $\Gamma(\mathbf{m},\tau)$, as noted in Subsection 3.A, is related to the measurement $M=g_2(\tau)$ through $((M-1)/\beta)G^2(\mathbf{m},0)$, which is $|G(\mathbf{m},\tau)|^2$. Therefore we have

$$\begin{aligned}\Gamma^{\delta}(\mathbf{m},\tau) &= [G(\mathbf{m},\tau) + G^{\delta}(\mathbf{m},\tau)][\bar{G}(\mathbf{m},\tau) + \bar{G}^{\delta}(\mathbf{m},\tau)]\\ &\quad - G(\mathbf{m},\tau)\bar{G}(\mathbf{m},\tau) \approx G^{\delta}(\mathbf{m},\tau)\bar{G}(\mathbf{m},\tau)\\ &\quad + G(\mathbf{m},\tau)\bar{G}^{\delta}(\mathbf{m},\tau) = \Gamma_1^{\delta}(\mathbf{m},\tau) + \Gamma_2^{\delta}(\mathbf{m},\tau),\end{aligned} \tag{12}$$

where $\Gamma^{\delta}(\mathbf{m},\tau)$ is real. Substituting $G^{\delta}(\mathbf{m},\tau) = \Gamma_1^{\delta}(\mathbf{m},\tau)/\bar{G}(\mathbf{m},\tau)$ in Eq. (11) we get

$$\int_{\partial\Omega} \frac{\Gamma_1^{\delta}(\mathbf{m},\tau)}{\bar{G}(\mathbf{m},\tau)} q^{+} \mathrm{d}^{n-1}r = \int_{\Omega} \mu_a^{\delta}(\mathbf{r}) G(\mathbf{r},\tau)\psi(\mathbf{r},\tau)\mathrm{d}^{n}r. \quad (13)$$

Similarly

$$\int_{\partial\Omega} \frac{\Gamma_2^{\delta}(\mathbf{m},\tau)}{G(\mathbf{m},\tau)} q^{+} \mathrm{d}^{n-1}r = \int_{\Omega} \mu_a^{\delta}(\mathbf{r}) \bar{G}(\mathbf{r},\tau)\bar{\psi}(\mathbf{r},\tau)\mathrm{d}^{n}r. \quad (14)$$

Therefore using the fact that $q^{+} = \delta(\mathbf{m}-\mathbf{m}_i)$, where $\mathbf{m}_i$ gives the ith detector location, we can write [by combining Eqs. (13) and (14)]

$$\Gamma^{\delta}(\mathbf{m}_i,\tau) = \mathrm{Re}\left\{ \bar{G}(\mathbf{m}_i,\tau) \int_{\Omega} \mu_a^{\delta}(\mathbf{r}') G(\mathbf{r}',\tau) G_R^{\psi}(\mathbf{r}',\mathbf{m}_i,\tau)\mathrm{d}^{n}r' \right\}, \quad (15)$$

where $G_R^{\psi}(\mathbf{r},\mathbf{m}_i,\tau)$ is the Green's function for the adjoint equation given by Eqs. (9) and (10). Here Re denotes "real part of."

Both $G^{\delta}(\mathbf{m}_i,\tau)$ and $\Gamma^{\delta}(\mathbf{m}_i,\tau)$ can also be obtained by solving the Frechet derivative operator [Eqs. (7) and (8)]. Through this route we obtain $\Gamma^{\delta}(\mathbf{m}_i,\tau)$ as

$$\Gamma^{\delta}(\mathbf{m}_i,\tau) = \mathrm{Re}\left\{ \bar{G}(\mathbf{m}_i,\tau) \int_{\Omega} \mu_a^{\delta}(\mathbf{r}') G(\mathbf{r}',\tau) G^{\Gamma}(\mathbf{m}_i,\mathbf{r}',\tau)\mathrm{d}^{n}\mathbf{r}' \right\}. \quad (16)$$

Comparing Eqs. (15) and (16) we get

$$G_R^{\psi}(\mathbf{r}',\mathbf{m}_i,\tau) = G^{\Gamma}(\mathbf{m}_i,\mathbf{r}',\tau). \quad (17)$$

Equation (17) is a reciprocity relation which asserts that the measurement made at $\mathbf{m}_i$ with source at $\mathbf{r}'$ [i.e., $G^{\Gamma}(\mathbf{m}_i,\mathbf{r}',\tau)$] is equal to the measurement made at $\mathbf{r}'$ with the source at $\mathbf{m}_i$ [i.e., $G_R^{\psi}(\mathbf{r}',\mathbf{m}_i,\tau)$]. Using Eq. (17) in Eq. (15) we get

$$\frac{\partial\Gamma(\mathbf{m}_i,\tau)}{\partial\mu_a^{\delta}(\mathbf{r}')} = \mathrm{Re}\{\bar{G}(\mathbf{m}_i,\tau) G(\mathbf{r}',\tau) G_R^{\psi}(\mathbf{r}',\mathbf{m}_i,\tau)\}. \quad (18)$$

2. Jacobian with Respect to D_B

The Frechet derivative of the forward propagation equation [Eqs. (2) and (3)] with respect to D_B is

$$\nabla\cdot D\nabla G^{\delta}(\mathbf{r},\tau) - (\mu_a + 2\mu_s' k_0^2 D_B\tau) G^{\delta}(\mathbf{r},\tau) = 2\mu_s' k_0^2 D_B^{\delta}\tau G(\mathbf{r},\tau), \quad (19)$$

with the boundary condition

$$G^{\delta}(\mathbf{r},\tau) + D\frac{\partial G^{\delta}(\mathbf{r},\tau)}{\partial n} = 0. \quad (20)$$

Following a similar procedure as in Subsection 3.B.1 we can easily see that the Jacobian of $\Gamma(\mathbf{m}_i,\tau)$ with respect to D_B is

$$\frac{\partial\Gamma(\mathbf{m}_i,\tau)}{\partial D_B^{\delta}(r')} = \mathrm{Re}[2\mu_s' k_0^2 \tau \bar{G}(\mathbf{m}_i,\tau) G_R^{\phi}(\mathbf{r}',\mathbf{m}_i,\tau) G(\mathbf{r}',\tau)]. \quad (21)$$

Here G_R^{ϕ} solves the adjoint of Eqs. (19) and (20), which is

$$\nabla\cdot D\nabla\phi(\mathbf{r},\tau) - (\mu_a + 2\mu_s' k_0^2 D_B\tau)\phi(\mathbf{r},\tau) = 0, \quad (22)$$

with the boundary condition

$$\phi(\mathbf{r},\tau) + D\frac{\partial\phi(\mathbf{r},\tau)}{\partial n} = q^{+}. \quad (23)$$

C. Jacobian for the Two Measurements M_1 and M_2 Derived from $\Gamma(\mathbf{m},\tau)$

Since M_1 and M_2 are obtained from $\Gamma(\mathbf{m},\tau)$ by integrating over different intervals of τ, the procedure to obtain either $\partial M_i/\partial\mu_a$ or $\partial M_i/\partial D_B$ is similar. We denote the perturbation equation connecting $E(\mathbf{m},\tau)$, the perturbation in $\Gamma(\mathbf{m},\tau)$, to the perturbation in p, the property of which is either μ_a or D_B, as

$$\sum_{j=1}^{N} \frac{\partial\Gamma(\mathbf{m}_k,\tau)}{\partial p_j}\Delta p_j = E(\mathbf{m}_k,\tau), \qquad k = 1,\ldots m. \quad (24)$$

Here m gives the number of measurements, N is the number of nodes in the domain Ω, and $E(\mathbf{m}_k,\tau)$ is the perturbation in the measurement $\Gamma_i(\mathbf{m}_k,\tau)$. We integrate Eq. (24) with respect to τ, take the integral inside the derivative operator, use M_i to denote $\int_{\tau_1}^{\tau_2}\Gamma(\mathbf{m}_k,\tau)\mathrm{d}\tau$ (where $i=1$ or 2 depending on whether τ_1 or τ_2 defines the first or the second interval of integration) and obtain

$$\sum_{j=1}^{n} \frac{\partial M_i}{\partial p_j}\Delta p_j^{av} = \Delta M_i, \quad (25)$$

where Δp_j^{av} is the mean value of Δp_j. In Eq. (25), the matrix $[\partial M_i/\partial p_j]$ is the Jacobian for measurement M_i (either M_1 or M_2) with respect to the property p (either μ_a or D_B). This Jacobian is constructed by integrating the derivatives given by Eqs. (18) and (21). It is seen that for the measurement M_1, the values of the derivative with respect to μ_a are larger; and for M_2 the same is true for derivatives with respect to D_B.

D. Jacobian for the Measurement $\Gamma(\mathbf{r},\tau)$ with Respect to $\langle\Delta r^2(\mathbf{r},\tau)\rangle$

We compute the Jacobian for the measurement $\Gamma(\mathbf{r},\tau_i)$ for $\tau=\tau_i$, a typical value of time τ. This Jacobian can be used to reconstruct $\langle\Delta r^2(\mathbf{r},\tau_i)\rangle$ using the inversion procedure discussed in Section 4. From the measurement vector $\{\Gamma(\mathbf{r},\tau_i)\}$ for a range of τ values and $\mathbf{r}\in\partial\Omega$ and using this Jacobian we recover the time varying $\langle\Delta r^2(\mathbf{r},\tau)\rangle$ for $\mathbf{r}\in\Omega$.

The Frechet derivative of the forward propagation equation [Eq. (2)] with respect to a perturbation in $\langle\Delta r^2(\mathbf{r},\tau)\rangle$ denoted by $\langle\Delta r^2(\mathbf{r},\tau_i)\rangle^{\delta}$ is

$$\nabla\cdot D\nabla G^{\delta}(\mathbf{r},\tau_i) - \left(\mu_a + \tfrac{1}{3}\langle\Delta r^2(\mathbf{r},\tau_i)\rangle k_0^2\mu_s'\right) G^{\delta}(\mathbf{r},\tau_i) = \tfrac{1}{3}k_0^2\mu_s'\langle\Delta r^2(\mathbf{r},\tau_i)\rangle^{\delta} G(\mathbf{r},\tau_i), \quad (26)$$

with the boundary condition

$$D\frac{\partial G^{\delta}(\mathbf{r},\tau_i)}{\partial n}+G^{\delta}(\mathbf{r},\tau_i)=0. \tag{27}$$

The adjoint of the above equation is

$$\nabla\cdot D\nabla\psi-\left(\mu_a+\tfrac{1}{3}\langle\Delta r^2(\mathbf{r},\tau_i)\rangle k_0^2\mu_s'\right)\psi=0, \tag{28}$$

with the boundary condition

$$D\frac{\partial\psi(\mathbf{r},\tau_i)}{\partial n}+\psi(\mathbf{r},\tau_i)=q^{+}. \tag{29}$$

With the procedure used in Subsection 3.B.1 we can easily compute the derivative of $\Gamma(\mathbf{m},\tau_i)$ with respect to $\langle\Delta r^2(\mathbf{r},\tau)\rangle$ as

$$\frac{\partial\Gamma(\mathbf{m}_i,\tau_i)}{\partial\langle\Delta r^2(\mathbf{m}_i,\tau_i)\rangle}=\mathrm{Re}\left\{\tfrac{1}{3}k_0^2\mu_s'\bar{G}(\mathbf{m}_i,\tau)G(\mathbf{r}',\tau_i)G_R^{\psi}(\mathbf{r}',\mathbf{m}_i,\tau_i)\right\}. \tag{30}$$

Here $G_R^{\psi}(\mathbf{r}',\mathbf{m}_i,\tau_i)$ is the Green's function for the adjoint system given by Eqs. (28) and (29).

4. ITERATIVE RECONSTRUCTION ALGORITHM

Figure 4 gives the block diagram of the proposed reconstruction algorithm. To start, the initial guesses of the properties of the medium such as $\mu_a(\mathbf{r})$, $\mu_s'(\mathbf{r})$, and $D_B(\mathbf{r})$ are given as inputs which are used in the forward propagation equation [Eqs. (2) and (3) discretized using the FEM] to compute $G(\mathbf{r},\tau)$. From $G(\mathbf{m},\tau)$ one can compute the measurements $\Gamma(\mathbf{m},\tau)$ and M by using Eqs. (5) and (6). The algorithm is also supplied with the experimental measurements M^e (specifically M_1^e and M_2^e) and $\{\Gamma^e(\mathbf{m}_i,\tau_i)\}$ for a set of τ_i values for each detector position $\mathbf{m}_i$. In our work the experimental data are numerically simulated using a finer mesh. As indicated in Subsection 3.A, the experiments give the normalized intensity autocorrelation which should be supplemented by a set of intensity measurements to compute $\Gamma(\mathbf{m},\tau)$ and M.

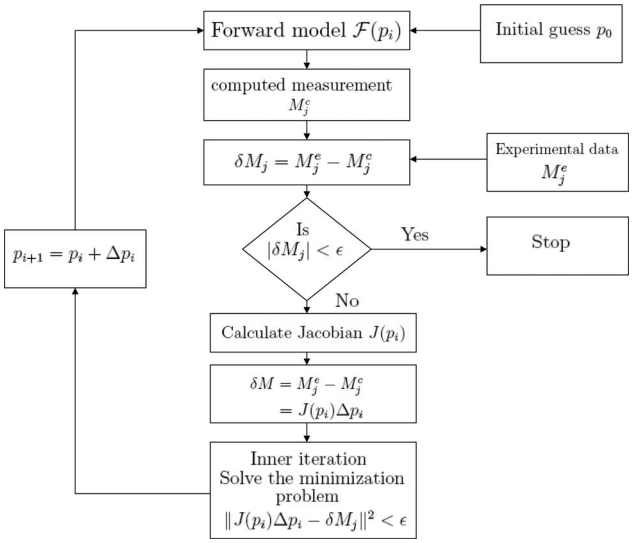

Fig. 4. Iterative reconstruction algorithm: The inputs to the algorithm are the initial guess of the property p_0 (either μ_a or D_B) and the experimental measurement M_j^e (either M_1^e or M_2^e). The algorithm has an outer and inner loop. In the inner loop the perturbation equation is solved to update the property p_i. In the outer loop the perturbation equation is itself updated.

From measurements M_1 and M_2 we reconstruct μ_a and D_B, respectively. Denoting by ΔM_1 and ΔM_2 the differences $M_1^e-M_1^c$ and $M_2^e-M_2^c$, where M_1^c and M_2^c are the computed measurements obtained from the current guess of the properties, we set up the perturbation equations $J_{\mu_a}\Delta\mu_a=\Delta M_1$ and $J_{D_B}\Delta D_B=\Delta M_2$. These perturbation equations are normalized by premultiplying by J^T, and after adding a suitable regularization parameter λ, they are written as

$$(J_{\mu_a}^T J_{\mu_a}+\lambda_1 I)\Delta\mu_a=J_{\mu_a}^T\Delta M_1, \tag{31}$$

$$(J_{D_B}^T J_{D_B}+\lambda_2 I)\Delta D_B=J_{D_B}^T\Delta M_2. \tag{32}$$

These are solved for $\Delta\mu_a$ and ΔD_B by recasting them as minimization problems, where $\|(J^TJ+\lambda I)\Delta p-J^T\Delta M\|^2=\epsilon$ is minimized by adjusting the parameter Δp. This is done in the inner loop of the iteration algorithm. The outputs from the inner iteration, either $\Delta\mu_a$ or ΔD_B, are used to update these properties to continue the algorithm in the outer loop, which requires updating Eqs. (31) and (32) by recomputing the Jacobians and ΔM_1 and ΔM_2. The algorithm is stopped when $\|\Delta M\|$ goes below a certain preset small value.

We sort the boundary measurements $\{\Gamma(\mathbf{m}_i,\tau_j)\}$ into sets $\{\Gamma(\mathbf{m}_i,\tau)\}_{\tau=\tau_j}$. Each set is used to set up the regularized perturbation equation similar to Eq. (31) and (32) as

$$(J_{\langle\Delta r^2(\mathbf{r},\tau_j)\rangle}^T J_{\langle\Delta r^2(\mathbf{r},\tau_j)\rangle}+\lambda_3 I)\Delta\langle\Delta r^2(\mathbf{r},\tau_j)\rangle=J_{\langle\Delta r^2(\mathbf{r},\tau_j)\rangle}^T\Delta\Gamma(\mathbf{m},\tau_j). \tag{33}$$

Equation (33) is inverted for $\Delta\langle\Delta r^2(\mathbf{r},\tau_j)\rangle$ which is used to update the current value of $\langle\Delta r^2(\mathbf{r},\tau_j)\rangle$. On convergence, we reconstruct the distribution of $\langle\Delta r^2(\mathbf{r},\tau_j)\rangle$ for $\tau=\tau_j$. By repeating the above iteration for all values of $\tau=\tau_j$ in the range of measurement of $g_2(\mathbf{m},\tau)$, we recover the complete time variation of $\langle\Delta r^2(\mathbf{r},\tau)\rangle$ for all $\mathbf{r}\in\Omega$.

5. NUMERICAL SIMULATIONS, RESULTS, AND DISCUSSION

A. Recovery of μ_a and D_B from Measurements M_1 and M_2

The object used in our numerical simulations is circular, taken as the cross-section of a cylinder of diameter 8 cm. The background optical and mechanical properties are kept as $\mu_a^b=0.001\ \mathrm{cm}^{-1}$, $\mu_s'^b=8\ \mathrm{cm}^{-1}$, and $D_B^b=0.1\times10^{-8}\ \mathrm{cm}^2/\mathrm{s}$. There are two circular inhomogeneous inclusions in this object of diameter 1.8 cm, one an absorption inhomogeneity of value $0.004\ \mathrm{cm}^{-1}$ centered at (–2.5 cm, 0 cm) and the other a D_B-inhomogeneity of $0.4\times10^{-8}\ \mathrm{cm}^2/\mathrm{s}$ at (2.5 cm, 0 cm). (The object is assumed to be centered at the origin of the coordinate axes.) Therefore the inclusions in the background are

$$\mu_a(x,y)=0.004\ \mathrm{cm}^{-1}\ \text{if}\ \sqrt{(x+2.5)^2+(y)^2}\leqslant 0.9,$$

$$D_B(x,y)=0.4\times10^{-8}\ \mathrm{cm}^2/\mathrm{s}\ \text{if}\ \sqrt{(x-2.5)^2+(y)^2}\leqslant 0.9.$$

To generate numerically the experimental data, Eqs. (2) and (3) are discretized using the FEM with 1933 nodes and 3723 triangular linear elements. For a collimated source on the boundary (which effectively means a point source inside the object at a distance of one transport mean free path from the boundary) 40 detectors are placed equi-angularly on either side of the diametrically opposite point to the source location, to cover an overall angle of 320°. The discretized forward equation is solved for $G(\mathbf{r},\tau)$ for τ ranging from $\tau=10^{-9}$ s to $\tau=10^{-3}$ s. From these, $\Gamma(\mathbf{r},\tau)$ are calculated for $\mathbf{r}\in\partial\Omega$ at all the detector locations, and the experimental data sets are generated by adding 1% Gaussian noise to $\Gamma(\mathbf{m},\tau)$. Particular measurements M_1 and M_2 are computed from the noisy $\Gamma(\mathbf{m},\tau)$. The above procedure is repeated by rotating the source–detector combination in unison by steps of 10° to gather 36 sets of 40 readings each.

For inversion of data we use a coarser mesh, discretizing the domain with 1243 nodal points and 2376 triangular elements. We start the reconstruction algorithm (see Fig. 4) with an initial guess of the properties μ_a and D_B, which are their background values. As mentioned before, the measurement M_1 is used to recover μ_a and M_2 to recover D_B. The Jacobians $\partial M_1^i/\partial\mu_a^j$ and $\partial M_2^i/\partial D_B^j$ are constructed for use in the iterative algorithm described in Section 4. Compared to these, the Jacobians $\{\partial M_2^i/\partial\mu_a^j\}$ and $\{\partial M_1^i/\partial D_B^j\}$ are found to be very small, proving that M_1 and M_2 are not sensitive to changes in D_B and μ_a, respectively. The whole set of data, which is the number of detector readings from all the views, is input to the reconstruction algorithm along with the initial guess of the properties and the Jacobians. The updates for μ_a and D_B are computed using the inner iteration. The algorithm converges in about 20 iterations of the outer loop when $\|\Delta M_i\|$ is reduced to less than 10^{-12}.

Gray level plots of the original μ_a and D_B distributions are shown in Figs. 5(a) and 5(b), respectively. The recovered $\mu_a(\mathbf{r})$ from M_1 is shown in Fig. 6 [the gray level plot in (a) and the cross-sections through the center of the inhomogeneity of the original and the recovered distributions in (b)]. Similarly the recovered $D_B(\mathbf{r})$ distribution from M_2 is shown in Fig. 7. It is seen that the quantitative accuracy of the inhomogeneous inclusions recovered including their locations is very good, even though the spatial resolution of the recovered inclusion seems to be poor. The loss of spatial resolution is due primarily to the diffusion of light.

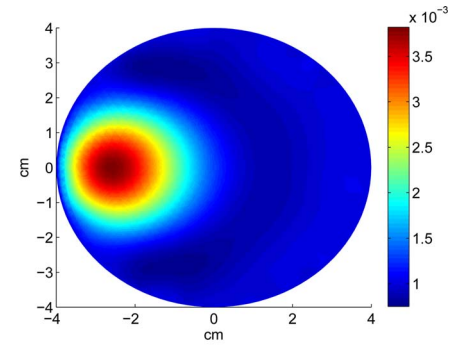

(a)

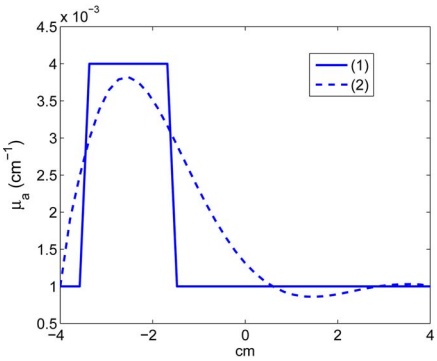

(b)

Fig. 6. (Color online) Reconstructed absorption coefficient distribution (cm^{-1}) (a) gray-level plot; (b) cross-sectional plots through the centers of the inhomogeneities in (a) as well as the original inhomogeneous object of Fig. 6(a).

Figures 8(a) and 8(b) show the recovered $D_B(\mathbf{r})$ and $\mu_a(\mathbf{r})$ from measurements M_1 and M_2, respectively. The Jacobians used here are (1) $\{\partial M_2/\partial\mu_a\}$ for recovering μ_a from M_2 and (2) $\{\partial M_1/\partial D_B\}$ for recovering D_B from M_1. The reconstructed D_B and μ_a are positioned at the μ_a and D_B inhomogeneities, respectively, of the original object. In this sense these reconstructions show the residuals of the insensitive parameters recovered from these measure-

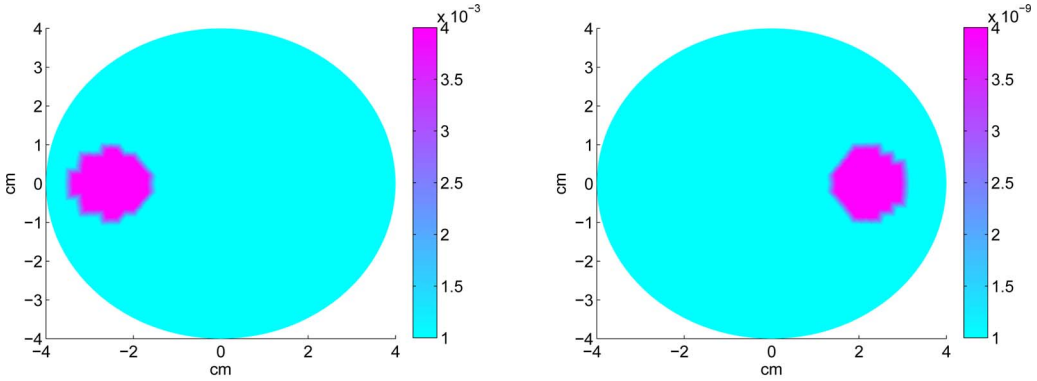

(a) (b)

Fig. 5. (Color online) Original object used in the simulations: (a) absorption coefficient (cm^{-1}) distribution; (b) particle diffusion coefficient distribution (cm^2/sec).

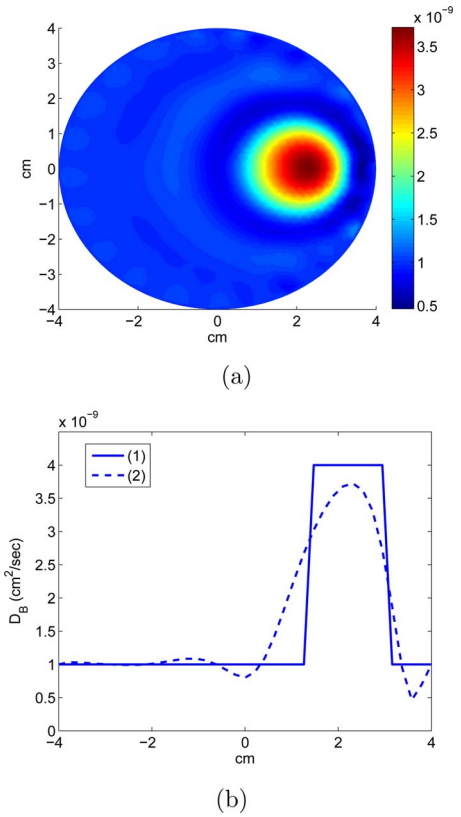

Fig. 7. (Color online) Reconstructed particle diffusion coefficient distribution (cm^2/sec) (a) gray-level plot; (b) cross-sectional plots through the centers of the inhomogeneities in (a) (dashed curve) as well as the original inhomogeneous object of Fig. 6(b) (solid curve).

ment types. We refer to them as cross-talks in the original reconstructions. It is seen that the cross-talk terms are very small compared with the actual reconstructions.

We observe that when the noise in the measurement is increased beyond 1%, the recovery is noisy, and therefore quantitative accuracy and position of the inhomogeneities cannot be guaranteed. Further, it is seen that the possible spatial resolution in the reconstruction is affected by noise in data. In addition it is noted that noise pushes up the minimum contrast needed in the inhomogeneity for it to be discernible in the reconstruction.

B. Recovery of $\langle \Delta r^2(\mathbf{r},\tau)\rangle$ from the Measurement $\Gamma(\mathbf{m},\tau)$

The object used here is similar to the one employed earlier. The background optical properties are the same as before ($\mu_a = 0.01$ cm^{-1} and $\mu_s' = 8$ cm^{-1}) and the mechanical property is defined using $\langle \Delta r^2(\mathbf{r},\tau)\rangle$ as explained below. Here $\langle \Delta r^2(\mathbf{r},\tau)\rangle$ is assumed to have a nonlinear variation with τ which is assumed to follow the relation [25]

$$\langle \Delta r^2(\mathbf{r},\tau)\rangle = r_0^2(\mathbf{r})\{1 - \exp[(-\tau/\tau_d)^{\alpha}]^{1/\alpha}\}(1 + 6D_1\tau/r_0^2). \tag{34}$$

Here $r_0(\mathbf{r})$ is a constant for a particular spatial location inside the object which defines the mechanical stiffness at location $\mathbf{r}$ (which defines the first plateau of the $\langle \Delta r^2(\mathbf{r},\tau)\rangle$ versus τ map), and τ_d is the time constant for the growth of $\langle \Delta r^2(\mathbf{r},\tau)\rangle$ with τ, which is given by $\tau_d = r_0^2/6D_B$. The values of D_1 and α are taken to be 10^{-12} cm^2/s and 0.28, respectively.

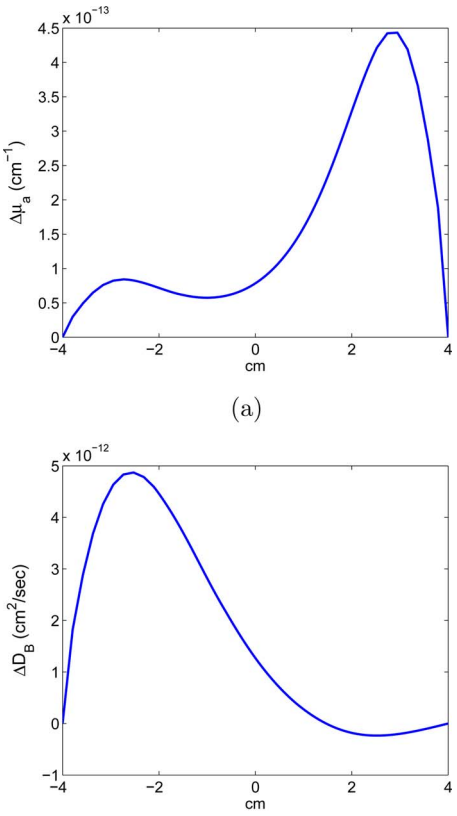

Fig. 8. (Color online) These reconstructions give the cross-talk in the reconstructions and are seen to be less than 1% of the correctly recovered D_B and μ_a. (a) The cross-sectional plot through the recovered change in absorption coefficient ($\Delta\mu_a = \mu_a(\mathbf{r}) - \mu_a^b$) from measurement M_2 using the Jacobian $\{\partial M_2/\partial \mu_a\}$.(b) The cross-sectional plot through the recovered change in particle diffusion coefficient [$\Delta D_B = D_B(\mathbf{r}) - D_B^b$] from measurement M_1 using the Jacobian $\{\partial M_1/\partial D_B\}$.

The background mechanical property is also fixed by defining $r_0(\mathbf{r})$ and τ_d. In the simulations r_0 for the background tissue is fixed at $r_0 = 7\times10^{-7}$ cm and τ_d is varied from 8.33×10^{-5} to 8.33×10^{-6} s by selecting D_B appropriately.

The object used in the simulations has two circular inhomogeneous inclusions of diameter 1.4 cm each. The constants r_0 and τ_d for these regions are kept as

$$r_0(x,y) = \begin{cases} 1.5811\times10^{-7}\ \text{cm} & \text{if } \sqrt{(x+2.5)^2+(y)^2} \le 0.7 \\ 5\times10^{-7}\ \text{cm} & \text{if } \sqrt{(x-2.5)^2+(y)^2} \le 0.7 \end{cases}. \tag{35}$$

The corresponding values of τ_d for $D_B = 1\times10^{-9}$ cm^2/s are given by

$$\tau_d(x,y) = \begin{cases} 4.1667\times10^{-6}\ \text{s} & \text{if } \sqrt{(x+2.5)^2+(y)^2} \le 0.7 \\ 4.1667\times10^{-5}\ \text{s} & \text{if } \sqrt{(x-2.5)^2+(y)^2} \le 0.7 \end{cases}. \tag{36}$$

We denote the relatively high stiffness region centered at $(-2.5, 0)$ as inhomogeneity 1 and the region centered at

(2.5,0) with stiffness close to that of background as inhomogeneity 2. A typical variation of $\langle \Delta r^2(\mathbf{r},\tau)\rangle$ with respect to τ is shown in Fig. 9 with $\mathbf{r}$ a point in the homogeneous background medium of the object.

As before the experimental data are generated by first numerically solving Eqs. (2) and (3) using FEM discretization with 1933 nodes and 3723 elements for $G(\mathbf{r},\tau)$ and then computing $\Gamma(\mathbf{r},\tau)$ from $G(\mathbf{r},\tau)$. The measurement is $\Gamma^e(\mathbf{m},\tau)=\Gamma(\mathbf{m},\tau)+$noise, where noise is 1% Gaussian. At each detector τ is varied from $\tau_{min}=10^{-6}$ s to $\tau_{max}=10$ s, giving a total of 40 samples of $\Gamma^e(\mathbf{m},\tau)$.

For inversion, we use a coarser mesh than in the previous case (1243 nodal points and 2376 triangular elements). We use the same reconstruction algorithm as used earlier, and the initial values used for the unknown $\langle \Delta r^2(\mathbf{r},\tau)\rangle$ correspond to its assumed background values. The required sensitivity matrices $\partial\Gamma(\mathbf{m},\tau_i)/\partial\langle \Delta r^2(\mathbf{r},\tau)\rangle$ are calculated for each value of τ_i (for each τ_i we get one Jacobian matrix), and the reconstruction proceeds using the steps described in the algorithm of Fig. 4. For a typical value of τ_i (say $\tau_i=10^{-6}$ s) the algorithm takes 30 iterations to converge, giving a reconstruction of $\langle \Delta r^2(\mathbf{r},\tau)\rangle$ at $\tau=\tau_i$ s, which is a spatial distribution of the parameter at the time selected. Repeating this we generate sets of $\langle \Delta r^2(\mathbf{r},\tau)\rangle$ reconstructions for τ going from $\tau=10^{-6}$ s to $\tau=10$ s.

A typical reconstruction of $\langle \Delta r^2(\mathbf{r},\tau)\rangle$ at $\tau=6\times10^{-5}$ s is shown in Fig. 10(a) (contour plot) with a cross-section through the inhomogeneity shown in Fig. 10(b). It is seen that the reconstruction is fairly accurate in both the inhomogeneities. However, we find that if the contrast in the inhomogeneity decreases below 50% of the background value [in $\langle \Delta r^2(\mathbf{r},\tau)\rangle$] the algorithm fails to reconstruct the inhomogeneity. Spatial resolution of the recovery is once again poor due to the diffusive propagation of light through the object. Figure 11 shows the plot of variation of the recovered $\langle \Delta r^2(\mathbf{r},\tau)\rangle$ with respect to τ at $\mathbf{r}$ inside the inhomogeneities. For comparison the original variations at those typical points are also shown. It is seen that the quantitative accuracy of reconstruction is reasonably

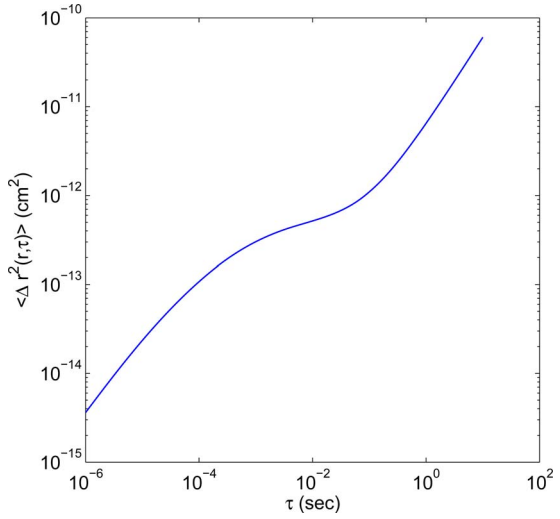

Fig. 9. (Color online) Typical variation of $\langle \Delta r^2(\mathbf{r},\tau)\rangle$ with τ for a homogeneous object ($r_0=7.0711\times10^{-7}$ cm, $D_B=10^{-9}$ cm^2/s, $D_1=10^{-12}$ cm^2/s, $\mu_a=0.01$ cm^{-1}, $\mu_s'=8$ cm^{-1}).

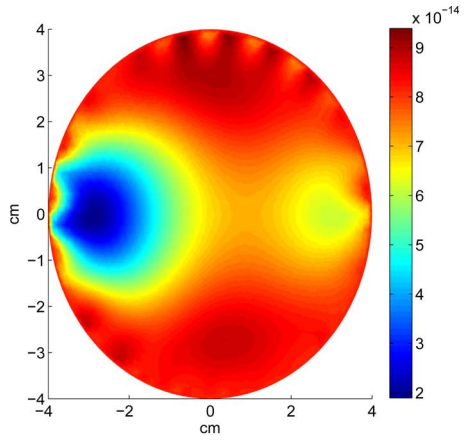

(a)

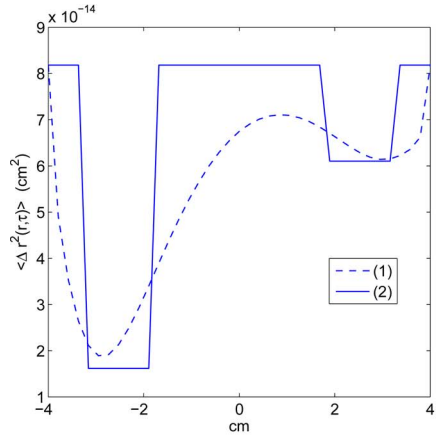

(b)

Fig. 10. (Color online) (a) Gray-level plot of reconstructed $\langle \Delta r^2(\mathbf{r},\tau)\rangle$ (cm^2) at $\tau=6\times10^{-5}$ s. (b) Cross-sectional plots through the centers of the inhomogeneities for the original (solid curve) and the reconstructed (dotted curves) $\langle \Delta r^2(\mathbf{r},\tau)\rangle$. The inhomogeneity at the left is designated as inhomogeneity 1 and the one at the right as inhomogeneity 2.

good. From the recovered $\langle \Delta r^2(\mathbf{r},\tau)\rangle$ we compute the storage modulus $G'(\omega)$ and loss modulus $G''(\omega)$ in the inclusions as [22]

$$G'(\omega)=|G^*(\omega)|\cos\left(\frac{\pi\alpha(\omega)}{2}\right), \tag{37}$$

$$G''(\omega)=|G^*(\omega)|\sin\left(\frac{\pi\alpha(\omega)}{2}\right), \tag{38}$$

where $G^*(\omega)$ is given by

$$|G^*(\omega)|\equiv\frac{K_BT}{\pi a\langle \Delta(\mathbf{r}^2,\tau)\rangle\Gamma(1+\alpha(\omega)}. \tag{39}$$

Here $\alpha(\omega)$ is the logarithmic slope of $\langle \Delta(\mathbf{r}^2,\tau)\rangle$ at $\tau=1/\omega$ and Γ is the gamma function.

The recovered storage and loss moduli in the first and the second inclusions are shown in Figs. 12(a) and 12(b), respectively.

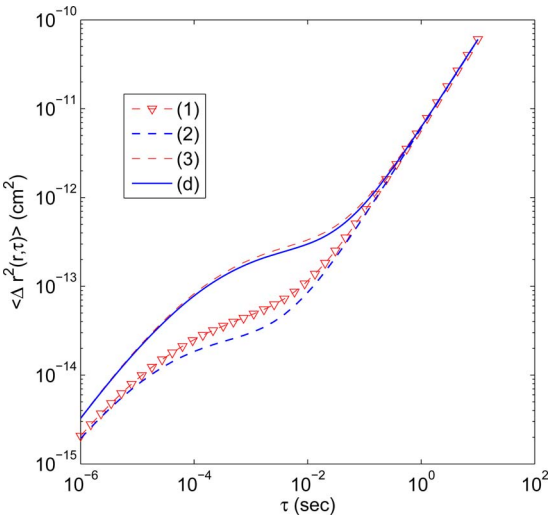

Fig. 11. (Color online) Reconstructed and original $\langle \Delta r^2(\mathbf{r},\tau)\rangle$ versus τ for the inhomogeneities 1 [(1) and (2), respectively] and 2 [(3) and (4), respectively].

6. TOWARD THE EXPERIMENTAL REALIZATION OF AN IMAGING SYSTEM

Since tissue is a highly scattering medium, the number of photons transmitted through an organ such as a breast being examined will be extremely small [28]. With this insignificantly small number of photons, to achieve sufficiently large SNRs in the measured intensity correlation is a challenging task. One should use a speckle averaging technique [29,30], employing a detector bundle consisting of an array of single mode fibers with each fiber capturing a single speckle to obtain an averaged $g_2(\tau)$ with an enhanced SNR. As noted earlier, in our simulations when the noise increased beyond 1% the quantitative accuracy of the recovery was greatly affected.

In DCT, the transmission geometry is seldom used, a backscattering geometry being prefered. With light input from a fiber at a particular position, the backscattered light is detected at a number of locations around the input such that the diffusive path of light in the object maps a certain volume of the object at a certain depth determined by the distance between the input and detector fibers.

Since the tissue is not an ergodic medium [31], the time autocorrelation estimate of $g_2(\tau)$ cannot be equated to the ensemble-averaged autocorrelation. In the literature [31] it is suggested that an ergodic medium consisting of beads suspended in water be sandwiched to the nonergodic medium studied to make a composite object which is ergodic. From the measured $g_2(\tau)$ for the sandwiched composite object, the contribution from the tissuelike object which is nonergodic is separated out.

In spite of the difficulties encountered in the measurement of $g_2(\tau)$ [32], DCT is currently demonstrated by many as a useful tool for *in vivo* blood flow measurement with potential medical diagnostic applications.

7. CONCLUSION

The study of propagation of field correlation of light through tissue and the corresponding inverse problem has the potential to provide noninvasive maps of the optical as well as mechanical properties of the tissue. This has obvious medical diagnostic applications, such as detecting the changes associated with the onset of cancer or other diseases. The objective of this work, proven through simulations, is the separate recovery of mechanical (represented by D_B, the particle diffusion coefficient) and optical (the absorption coefficient) properties from the measurements derived from the boundary intensity autocorrelation $g_2(\tau)$. We have devised two measurements M_1 and M_2 which are integrals of a function derived from the measured $g_2(\tau)$, the first going from $\tau=10^{-9}$ s to $\tau=10^{-7}$ s (smaller values of τ) and the second going from $\tau=10^{-6}$ s to $\tau=10^{-3}$ s (relatively larger values of τ). Through numerical simulations we confirmed that M_1 is sensitive to μ_a variations and insensitive to D_B variations and vice versa for M_2. We have constructed the Jacobian matrix for these measurements with respect to μ_a and D_B and used these in the recovery of these parameters. We have shown that μ_a and D_B can be separately reconstructed from measurements M_1 and M_2 employing the forward propagation operator for the amplitude autocorrelation in the reconstruction algorithm. The cross-talk (as defined earlier) in these reconstructions is negligible. The reconstructed accuracy of the inhomogeneities recovered is >90% for both μ_a and D_B. The location of the in-

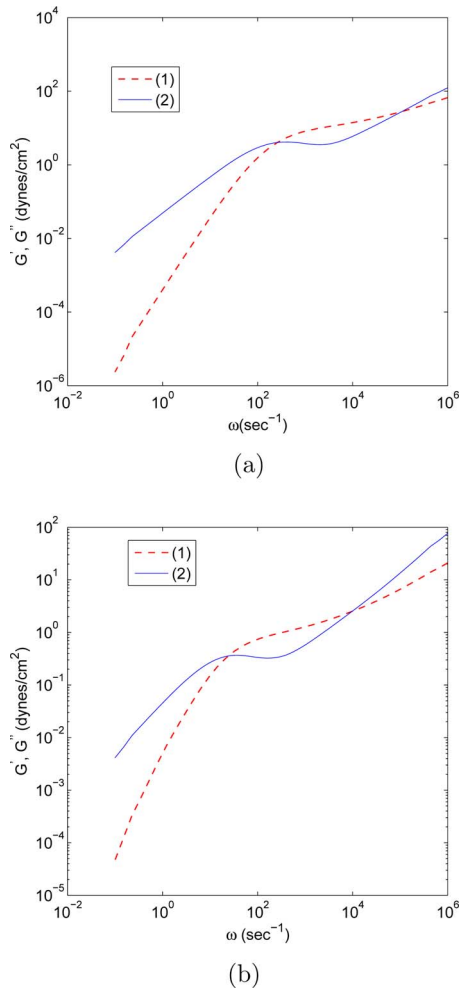

Fig. 12. (Color online) Reconstructed G' (dotted curve) and G'' (solid curve) for (a) inhomogeneity 1, (b) inhomogeneity 2.

homogeneity is accurately recovered, so long as the noise in the data is below 1%, even though the spatial resolution is affected by the diffusive nature of the $G_1(\tau)$ propagation in turbid media.

In addition, we have verified the possibility of a space-resolved recovery of $\langle \Delta r^2(\mathbf{r},\tau)\rangle$ from the boundary measurements of complete sets of $g_2(\tau)$ for all τ, in the case where the behavior of $\langle \Delta r^2(\mathbf{r},\tau)\rangle$ with τ is nonlinear, representing a viscoelastic tissuelike medium. At any inhomogeneous location in the object, the variation of $\langle \Delta r^2(\mathbf{r},\tau)\rangle$ with τ is recovered, from which $G'(\omega)$ and $G''(\omega)$, the storage and loss moduli, respectively, are extracted. This opens up the possibility of diagnosing regions with pathology on the basis of changes in $G'(\omega)$.

ACKNOWLEDGMENTS

Fruitful discussions with A. K. Sood as well as comments from the reviewer helped to improve the quality of this paper. This work was financially supported by the Department of Science and Technology Centre for Mathematical Biology, Indian Institute of Science, Bangalore, under a grant from the Department of Science and Technology, Government of India.

REFERENCES AND NOTES

1. D. J. Pine, D. A. Weitz, P. M. Chaikin, and E. Herbolzheimer, "Diffusing-wave spectroscopy," Phys. Rev. Lett. **60**, 1134–1137 (1988).
2. M. J. Stephen, "Temporal fluctuations in wave propagation in random media," Phys. Rev. B **37**, 1–5 (1988).
3. G. Maret and D. E. Wolf, "Multiple light scattering from disordered media. The effect of Brownian motion of scatterers," Z. Phys. B: Condens. Matter **65**, 409–413 (1987).
4. D. A. Weitz, D. J. Pine, P. N. Puxy, and R. J. A. Tough, "Non-diffusive Brownian motion studied by diffusing-wave spectroscopy," Phys. Rev. Lett. **63**, 1747–1750 (1989).
5. D. Bicuot and G. Maret, "Multiple light scattering in Taylor-Couette flow," Physica A **210**, 87–112 (1994).
6. W. Leutz and G. Maret, "Ultrasound modulation of multiply scattered light," Physica B **204**, 14–19 (1995).
7. G. Yao and L. V. Wang, "Theoretical and experimental studies in ultrasound modulated optical tomography-biological tissues," Appl. Opt. **39**, 659–664 (2000).
8. A. P. Gibson, J. C. Hebden, and S. R. Arridge, "Recent advances in diffuse optical imaging," Phys. Med. Biol. **50**, R1–R43 (2005).
9. D. A. Boas, D. H. Brooks, C. A. Dimarzio, M. Kilmer, R. J. Gaudette, and Q. Zhang, "Imaging the body with diffuse optical tomography," IEEE Signal Process. Mag. **18**, 57–75 (2001).
10. M. Heckmeier, S. E. Skipetrov, G. Maret, and R. Maynard, "Imaging of dynamic heterogeneities in multiple-scattering media," J. Opt. Soc. Am. A **14**, 185–191 (1997).
11. D. A. Boas, L. E. Campbell, and A. G. Yodh, "Scattering and imaging with diffuse temporal field correlation," Phys. Rev. Lett. **75**, 1855–1858 (1995).
12. D. A. Boas and A. G. Yodh, "Spatially varying dynamical properties of turbid media probed with diffusing temporal light correlation," J. Opt. Soc. Am. A **14**, 192–215 (1997).
13. M. Heckmeier and G. Maret, "Visualization of flow in multiple scattering liquids," EPL **34**, 257–262 (1996).
14. T. G. Mason and D. A. Weitz, "Optical measurements of the linear viscoelastic moduli of complex fluids," Phys. Rev. Lett. **74**, 1250–1253 (1995).
15. C. Usha Devi, R. S. Bharat Chandran, R. M. Vasu, and A. K. Sood, "Measurement of visco-elastic properties of breast-tissue mimicking materials using diffusing wave spectroscopy," J. Biomed. Opt. **12**, 034035(1–5) (2007).
16. T. Gisler and D. A. Weitz, "Tracer microrheology in complex fluids," Curr. Opin. Colloid Interface Sci. **3**, 586–592 (1998).
17. C. Zhou, G. Yu, D. Furuya, J. H. Greenberg, A. G. Yodh, and T. Durduran, "Diffuse correlation tomography of cerebral blood flow during cortical spreading depression in rat brain," Opt. Express **3**, 1125–1144 (2006).
18. C. Cheung, J. P. Culver, K. Takahashi, J. H. Greenberg, and A. G. Yodh, "In vivo cerbrovascular measurement combining diffuse near-infrared absorption and correlation spectroscopies," Phys. Med. Biol. **46**, 2053–2065 (2001).
19. E. Gratton, V. Toronov, U. Wolf, M. Wolf, and A. Webb, "Measurememt of brain activity by near-infrared light," J. Biomed. Opt. **10**, 011008–011013 (2005).
20. T. Durduran, R. Choe, G. Yu, C. Zhou, J. C. Tehou, B. J. Czerniecki, and A. G. Yodh, "Diffuse optical measurement of blood flow in breast tumors," Opt. Lett. **30**, 2915–2917 (2005).
21. A. H. Hielscher, A. D. Klose, and K. M. Hanson, "Gradient-based iterative image reconstruction sceheme for time-resolved optical tomography," IEEE Trans. Med. Imaging **18**, 262–271 (1999).
22. T. G. Mason, "Estimating the visco-elastic moduli of complex fluids using the generalized Stokes-Einstein equation," Rheol. Acta **39**, 371–378 (2000).
23. S. Sakadzic and L. V. Wang, "Correlation transfer and diffusion of ultrasound-modulated multiply scattered light," Phys. Rev. Lett. **96**, 163902 (2006).
24. S. Sakadzic and L. V. Wang, "Correlation transfer equation for multiply scattered light modulated by an ultrasonic pulse," J. Opt. Soc. Am. A **24**, 2797–2806 (2007).
25. M. Bellour, M. Skouri, J.-P. Munch, and P. Hebraud,"Brownian motion of particles embedded in a solution of giant micelles," Eur. Phys. J. E **8**, 431–436 (2002).
26. S. R. Arridge, "Topical review: optical tomography in medical imaging," Inverse Probl. **15**, R41–R93 (1999).
27. H. M. Varma, R. M. Vasu, and A. K. Nandakumaran, "Direct reconstruction of complex refractive index distribution from boundary measurement of intensity and normal derivative of intensity," J. Opt. Soc. Am. A **24**, 3089–3099 (2007).
28. B. Chance, ed., *Photon Migration in Tissues* (Plenum, 1989).
29. G. Dietsche, M. Ninck, C. Ortolf, J. Li, F. Jaillon, and T. Gisler, "Fiber-based multispeckle detection for time-resolved diffusing-wave spectroscopy: characterization and application to blood flow detection in deep tissue," Appl. Opt. **46**, 8506–8514 (2007).
30. F. Jaillon, J. Li, G. Dietsche, T. Elbert, and T. Gisler, "Activity of the human visual cortex measured non-invasively by diffusing-wave spectroscopy," Opt. Express **15**, 6643–6650 (2007).
31. F. Scheffold, S. E. Skipetrov, S. Romer, and P. Schurtenberger, "Diffusing wave spectroscopy of nonergodic media," Phys. Rev. E **63**, 061404 (2001).
32. It is assumed that the detector is fast enough to respond to the decay of $g_2(\mathbf{m},\tau)$. This can pose difficulties in the case where either the source–detector separation and/or the optical properties and MSD are so large that $g_2(\mathbf{m},\tau)$ decays very fast. For the simulations we did, corresponding to the average properties and size of human breast, boundary correlation decay is slow enough for measurement.